

3D Macro Physics and Light Odd-Z Element Production in O-C Shell Mergers: Implications for ^{40}K production and radiogenic heating inventories of rocky exoplanets

JOSHUA ISSA ,^{1,2} FALK HERWIG ,^{1,2} STEPHEN J. MOJZSIS ,^{3,4,5} AND MARCO PIGNATARI ,^{4,5,3,2}

¹ *Astronomy Research Centre, Department of Physics & Astronomy, University of Victoria, Victoria, BC, V8W 2Y2, Canada*

² *NuGrid Collaboration, <http://nugridstars.org>*

³ *Geoastronomy Research Group, Bayerisches Geoinstitut, Universität Bayreuth, Universitätsstraße 30, 95447 Bayreuth, Germany*

⁴ *HUN-REN Research Center for Astronomy and Earth Sciences (CSFK), 1121 Budapest, Konkoly Thege Miklós út 15-17, Hungary*

⁵ *CSFK, MTA Centre of Excellence, Budapest, Konkoly Thege Miklós út 15-17., H-1121, Hungary*

(Received September 23, 2025; Revised December 8, 2025; Accepted December 8, 2025)

Submitted to ApJ

ABSTRACT

The light odd-Z elements P, Cl, K, and Sc are underproduced in galactic chemical evolution models compared to spectroscopic observations of stars in the Milky Way. The most promising solution to this puzzle is that some massive stars experience O-C shell mergers boosting their yields through dynamic, convective-reactive nucleosynthesis. We report how convective macro physics based on 3D 4π hydrodynamic simulations impacts production in the O shell by post-processing the $M_{\text{ZAMS}} = 15 \text{ M}_{\odot}$, $Z = 0.02$ model from the NuGrid dataset. We explore a mixing downturn, boosted velocities, reduced ingestion rate, and convective quenching. Across 24 mixing cases, the pre-explosive yields for [P/Fe], [Cl/Fe], [K/Fe], and [Sc/Fe] are modified by $[-0.33, 0.23]$ dex, $[-0.84, 0.64]$ dex, $[-0.78, 1.48]$ dex, and $[-0.36, 1.29]$ dex, respectively. Cases with a convective downturn with the fastest ingestion rate have the largest enhancement, and production is non-monotonic with boosted velocities. Which reactions are most important for the convective-reactive element production pathways depends on the mixing case. We parameterize production of ^{40}K ($t_{1/2} = 1.248$ Gyr), an important radiogenic heat source for younger (2–3 Gyr) rocky planets and find a yield variation exceeding three orders of magnitude. This range of initial abundances for ^{40}K implies the early geodynamic behaviour of silicate mantles in rocky planets can differ greatly from that of Earth. These results underscore the importance of investigating the 3D macro physics of shell merger convection through hydrodynamic simulations to develop a predictive understanding of the origin and variability of the light odd-Z elements and the $^{40}\text{K}/\text{K}$ ratio in planet host stars.

Keywords: Massive stars (732) — Oxygen burning (1193) — Stellar convective shells (300) — Nuclear astrophysics (1129) — Exoplanets (498) — Planetary atmospheres (1244)

1. INTRODUCTION

The radiogenic isotope ^{40}K with a half-life of 1.248 Gyr is the dominant heat-producing nuclide for rocky exoplanets in the first few billion years of their geologic histories (e.g. C. O’Neill et al. 2020), with Earth as the baseline example (J. Korenaga 2008). Of the long-lived radionuclides present in silicate mantles of rocky planets, ^{40}K -driven radiogenic heating contributes to mantle convection that feeds into volcanism, the pri-

mary mechanism for transferring volatiles from planetary interiors to atmospheres. Variations in initial ^{40}K inventories directly affect the duration and intensity of volcanic degassing (L. Noack & D. Breuer 2014), particularly during the critical first 2–3 billion years when secondary atmosphere formation occurred when ^{40}K was still a dominant heat-producer (T. P. Fischer & A. Aiuppa 2020).

Therefore, any model of the geodynamic evolution of rocky exoplanets requires knowledge of the initial ^{40}K inventories. However, K belongs to a group of elements with a particularly uncertain production history. A long-standing problem has been that the light odd-Z

Corresponding author: Joshua Issa
 Email: joshuaissa@uvic.ca

elements P, Cl, K, and Sc are produced in insufficient quantities in galactic chemical evolution (GCE) models. Indeed, GCE models predict that the majority contribution for these elements comes from core-collapse supernovae (CCSNe), but they cannot match observed stellar abundances (e.g. T. Mishenina et al. 2017; N. Prantzos et al. 2018; C. Kobayashi et al. 2020). A recent realization has been that the light odd-Z elements are significantly produced during O-C shell merger in massive stars prior to a CCSN at all metallicities (T. Rauscher et al. 2002; C. Ritter et al. 2018a; L. Roberti et al. 2025), and GCE models including this effect parametrically can match stellar abundance observations.

Current K and by extension ^{40}K predictions from O-C shell mergers remain uncertain. A key source of uncertainty is the impact of macro physics of convection during the dynamic nucleosynthesis, possibly with feedback, as demonstrated recently for the *p*-process-production in O-C shell mergers (J. Issa et al. 2025). A ^{40}K production variability similar to that seen for *p*-process abundance predictions taking into account different scenarios of macro physics of convection based on stellar hydrodynamics simulations, could lead to divergent planetary atmospheric evolution pathways. Differences in composition and thickness of planet atmospheres depend on both the thermal state driving outgassing efficiency and the pressure-temperature conditions controlling volatile speciation (G. Ortenzi et al. 2020), creating potentially observable signatures in $\text{CO}_2/\text{H}_2\text{O}$ ratios and atmospheric oxidation states that future missions like the Habitable Worlds Observatory could detect (P. Liggins et al. 2022a). A predictive, quantitative understanding of ^{40}K production would remove a key roadblock in our ability to model the thermal evolution of silicate-metal exoplanets (E. A. Frank et al. 2014).

Not surprisingly, three-dimensional (3D) hydrodynamic simulations of the O shell where the nucleosynthesis occurs show very different mixing conditions compared to one-dimensional (1D) predictions using mixing length theory (MLT) (C. A. Meakin & D. Arnett 2006, 2007; S. Jones et al. 2017; T. Yoshida et al. 2019; R. Andrassy et al. 2020; N. Yadav et al. 2020; T. Yoshida et al. 2021; C. E. Fields & S. M. Couch 2021; F. Rizzuti et al. 2024). These simulations have shown that the radial mixing efficiency profile has a downturn as the convective boundary is approached, which is not captured in 1D models which predict the mixing should be nearly constant across the convective shell (C. A. Meakin & D. Arnett 2006, 2007; S. Jones et al. 2017). They also predict that the convective velocities could be larger by up to a factor of 30 or more than what is predicted by 1D models (S. Jones et al. 2017; R. Andrassy et al. 2020;

F. Rizzuti et al. 2024). Finally, convective quenching due to energy feedback from the ingestion of fresh fuel has been demonstrated in 3D simulations of H-ingestion in post-AGB (asymptotic giant branch; AGB) stars (F. Herwig et al. 2014), and the ingestion of C-shell material into the O shell may play a similar restricting role in O-C shell mergers (R. Andrassy et al. 2020).

These mixing conditions directly affect the nucleosynthesis as the O shell is a convective-reactive environment where the timescales for mixing and burning are comparable (C. Ritter et al. 2018a; N. Yadav et al. 2020; F. Rizzuti et al. 2024). F. Rizzuti et al. (2024) have shown in their 3D simulation of an O-C shell merger that all isotopes have significantly different results compared to 1D simulations.

Here we consider how the isotopes ^{31}P , $^{35,37}\text{Cl}$, $^{39,40,41}\text{K}$, and ^{45}Sc are produced in the O shell and how it is impacted by the mixing conditions. This extends the work done by J. Issa et al. (2025) that analyzed how the *p* nuclei are affected by the mixing conditions during the shell merger. We analyze the production of these nuclides, with special attention to K and its isotopes. While stellar spectral data of the host star can be used to infer plausible major element compositions of rocky exoplanets (e.g. R. J. Spaargaren et al. 2023), only GCE models can provide likely relative abundances of the radioactive nuclides (^{40}K , ^{232}Th , $^{235-238}\text{U}$), tied to the age of that system, that can be used to infer heat production in the interiors of rocky exoplanets (E. A. Frank et al. 2014). While indeed for Th it is possible to directly observe ^{232}Th in stars in the Milky Way disk, current spectroscopic observation uncertainties still hinder precise derivation of its abundances (e.g., R. B. Botelho et al. 2019; T. Mishenina et al. 2022, and references therein).

This paper is structured as follows. In §2, we describe our methodology, including the initial conditions from the NuGrid stellar model, the post-processed models with different mixing scenarios, and our approach for estimating final yields and reaction contributions. §3 presents our main results, focusing on the nucleosynthesis of light odd-Z isotopes and how different mixing conditions impact their production. In §4, we discuss the production of ^{40}K and its implications for heterogeneous pollution of the interstellar medium and radiogenic heating in rocky exoplanets. Finally, §5 provides our discussion and conclusions, highlighting the importance of mixing conditions for understanding the origin of light odd-Z elements, their impact on galactic chemical evolution models and radiogenic heating in rocky exoplanets.

2. METHODOLOGY

2.1. *The O-C shell merger model*

The radial stratification for the O shell multizone nucleosynthesis simulations in this paper are taken from the non-rotating, 1D $15 M_{\odot}$ $Z = 0.02$ massive star model from the NuGrid data set (C. Ritter et al. 2018b) calculated with the MESA stellar evolution code (B. Paxton et al. 2010) and post-processed with the multi-zone NuGrid code `mppnp` (M. Pignatari et al. 2016). This model does not have exponential-diffusive convective boundary mixing (B. Freytag et al. 1996; F. Herwig 2000) after the cessation of core He burning (which was explored in A. Davis et al. 2018). The evolution of the convection zones is shown in a Kippenhahn diagram (Figure 1) in J. Issa et al. (2025). The light odd-Z elements are mildly produced in the first convective O shell, which extends from $1.55 M_{\odot}$ to $1.95 M_{\odot}$ during a time interval $\log_{10}(t - t_{\text{end}})/\text{yr} = -1.76$ to -2.16 , but the O-C shell merger at $\log_{10}(t - t_{\text{end}})/\text{yr} = -3.85$ is the dominant source of the elements (C. Ritter et al. 2018a).

Table 1 summarizes the NuGrid model properties with O-C shell mergers from C. Ritter et al. (2018b). The 12, 15, and 20 M_{\odot} models show clear differences in the size of the merged shells Δm , duration of the merger Δt , and overproduction factors OP for $^{39-41}\text{K}$. However, both 15 M_{\odot} models with metallicities $Z = 0.01$ and $Z = 0.02$ are quite similar in all these properties, including in OP, although the $Z = 0.02$ model produces three times more ^{39}K by the end of the merger because of a higher initial mass fraction. This would suggest that initial stellar mass is more determinate of the merger and its nucleosynthesis than its metallicity. In fact, L. Roberti et al. (2025) shows that models with O-C shell mergers do not have a general trend in [K/Mg] across metallicities of $Z = 10^{-9}-10^{-2}$.

2.2. *Post-Processed Models*

We use the post-processed models from J. Issa et al. (2025) of the $15 M_{\odot}$ $Z = 0.02$ NuGrid model that implement insights from 3D hydrodynamic simulations to motivate mixing scenarios expressed in terms of mixing efficiency profiles that are different from the MLT 1D predictions. We focus solely on the $15 M_{\odot}$ $Z = 0.02$ model for this exploratory study as it has the largest production of the p nuclei (C. Ritter et al. 2018a) and $^{39-41}\text{K}$ (Table 1) for the merger models. These simulations use mass fractions from just before merger onset at $\log_{10}(t - t_{\text{end}})/\text{yr} = -3.845$ and a constant stellar structure, including mixing profile, from the onset at $\log_{10}(t - t_{\text{end}})/\text{yr} = -3.856$. This is run for 110 s, the same time between these moments, which corresponds to at least 2 – 3 convective turnovers which implies a

quasi-equilibrium state. All nucleosynthesis is captured with a network of 1470 isotopes.

The MLT mixing case with a mixing efficiency profile essentially constant across the O shell as taken from C. Ritter et al. (2018b). 3D simulations, however, predict a mixing efficiency downturn as the convective boundary is approached and an increased mixing efficiency compared to MLT (C. A. Meakin & D. Arnett 2007; S. Jones et al. 2017; R. Andrassy et al. 2020; C. E. Fields & S. M. Couch 2021; F. Rizzuti et al. 2024), to some degree depending on the uncertain hydrodynamic response to the ingestion and burning of additional nuclear fuel. Therefore, we implement the 3D-inspired mixing profile from S. Jones et al. (2017) that features a convective downturn, and boost the MLT velocities by factors of 1, 3, 10, and 50. The MLT and 3D-inspired cases are calculated with ingestion rates of $4 \times 10^{-5} M_{\odot}\text{s}^{-1}$, $4 \times 10^{-4} M_{\odot}\text{s}^{-1}$, $4 \times 10^{-3} M_{\odot}\text{s}^{-1}$, which are consistent with those adopted in the 3D simulations of R. Andrassy et al. (2020). The extent of the C shell is $0.8 M_{\odot}$, so for a post-processing simulation time of 110 s, the maximum ingestion rate would be $7 \times 10^{-3} M_{\odot}\text{s}^{-1}$ like C. Ritter et al. (2018a). Our fastest ingestion rate of $4 \times 10^{-3} M_{\odot}\text{s}^{-1}$ reflects a full merger and a case without ingestion is also included for reference. Quenched mixing cases are also considered by implementing a dip in the mixing efficiency profile. This may arise due to energy feedback in the middle of the shell at 4.95 Mm and partial merging of the shells at 7.5 Mm as 3D simulations suggest (R. Andrassy et al. 2020). Two quenching strengths expressed as dips in the profile to $10^{14} \text{ cm}^2\text{s}^{-1}$ and $10^{13} \text{ cm}^2\text{s}^{-1}$ are considered. The quenched mixing cases are calculated with an ingestion rate of $4 \times 10^{-3} M_{\odot}\text{s}^{-1}$ only. There are 4 MLT, 16 3D-inspired, and 4 quenched mixing cases for a total of 24 simulations. This reflects both our limited knowledge of and the intrinsically varying conditions in real 3D stars. The `mppnp` code treats mixing as a diffusive process and splits the operators of mixing and burning (M. Pignatari et al. 2016), so care has been taken that our post-processing models are converged with respect to spatial and temporal resolution. J. Issa et al. (2025) provides further explanation of all simulation details.

2.3. *Estimating Pre-Explosive Yields*

The post-processed models in this work are calculated only for the O shell without the rest of the star, including the merging C shell. Therefore, we must estimate the final yields if our mixing prescriptions were implemented into a full stellar evolution calculation. The final ejected mass of a species i is given by:

$$\text{EM}_i = \text{EM}_i^{\text{wind}} + \text{EM}_i^{\text{SN}}$$

M_{ZAMS}	Z_{ini}	Δm	Δt	$\langle X(\text{K}) \rangle_{\text{fin}}$	$\text{OP}(\text{K})$	$\langle X(\text{K}) \rangle_{\text{fin}}$	$\text{OP}(\text{K})$	$\langle X(\text{K}) \rangle_{\text{fin}}$	$\text{OP}(\text{K})$
$12 M_{\odot}$	0.01	$0.6 M_{\odot}$	0.029 h	2.48×10^{-4}	1.531	6.72×10^{-6}	1.362	1.49×10^{-6}	0.487
$15 M_{\odot}$	0.01	$1.52 M_{\odot}$	0.74 h	3.01×10^{-4}	1.98	3.24×10^{-5}	1.934	2.71×10^{-5}	1.63
$20 M_{\odot}$	0.01	$3.6 M_{\odot}$	5.43 h	2.28×10^{-4}	1.841	3.56×10^{-6}	0.895	7.01×10^{-7}	0.004
$15 M_{\odot}$	0.02	$1.43 M_{\odot}$	1.252 h	9.43×10^{-4}	2.028	5.85×10^{-5}	1.965	2.38×10^{-5}	1.305

Table 1. Properties of the merger and production of K for the NuGrid models with O-C shell mergers. The averaged mass fractions are within the maximum extent of the merger region and $\text{OP} = \log_{10}(\langle X_{\text{fin}} \rangle / \langle X_{\text{ini}} \rangle)$ where $\langle X_{\text{ini}} \rangle$ and $\langle X_{\text{fin}} \rangle$ are taken at the start and end of the merger. Note that the models have different initial mass fractions of $^{39-41}\text{K}$.

where $\text{EM}_i^{\text{wind}}$ are the yields from winds throughout stellar evolution and EM_i^{SN} are the ejected yields due to a supernova without explosive burning as described by C. Ritter et al. (2018b). Winds are taken from the surface abundances and are not affected by the mixing conditions in the O shell, and are the same as C. Ritter et al. (2018b), but the pre-explosive supernova yields are altered by the mixing conditions. Our assumption is that the ratio of the decayed mass fractions calculated in our models at $t = 110$ s to those in the C. Ritter et al. (2018b) O shell at $\log_{10}(t - t_{\text{end}})/\text{yr} = -3.856$ (the corresponding time in the NuGrid model) remains the same for all subsequent evolution across the whole O-C region. Since the convective turnover is shorter than the simulation time, this assumption is reasonable. This allows us to estimate what the yields of an entire stellar model would be if our 3D-inspired mixing conditions were used, although this neglects feedback effects that cannot be captured without full stellar evolution calculations. Therefore, these results are not meant as predictive yields, but rather an exploratory study of how mixing conditions may impact nucleosynthesis.

Following C. Ritter et al. (2018b), we use the delayed explosion mass cut of C. L. Fryer et al. (2012) to find $m = 1.619 M_{\odot}$ for our approximated yields:

$$\text{EM}_i^{\text{SN}} = \int_{1.619 M_{\odot}}^{2.95 M_{\odot}} X_i \cdot \text{ratio}_i dm + \int_{2.95 M_{\odot}}^{m_{\tau}} X_i dm$$

where X_i is the mass fraction of an element i , ratio_i is the ratio across the O shell of the decayed mass fractions for a model and C. Ritter et al. (2018b) for element i , m_{τ} is the extent of the star at collapse, and $1.619-2.95 M_{\odot}$ is the O-C merger region above the mass-cut. The mass fraction is calculated as the yield of a given species normalized to the total yield:

$$X_i = \text{EM}_i \div \sum_i^N \text{EM}_i \quad (1)$$

where N is the total number of species.

The final results are calculated in square bracket notation against C. Ritter et al. (2018b) (indicated by the

subscript $\text{ref} = \odot$) and the solar measurements from M. Asplund et al. (2009) (ref = \odot):

$$[\text{X}/\text{Y}]_{\text{ref}} = \log_{10}(\text{X}/\text{Y})_{\text{norm}} - \log_{10}(\text{X}/\text{Y})_{\text{ref}}$$

where X and Y are mass fractions calculated with Eq. (1), and the subscript norm indicates what is being compared to the reference value.

2.4. Estimating Reaction Contribution

The reaction flux f_{ij} is defined as the net flux of the reaction between species i and j :

$$f_{ij} = \frac{X_i X_j}{A_i A_j} \rho N_A \left(\langle \sigma v \rangle_{ij} - \langle \sigma v \rangle_{ji} \right)$$

where X is the mass fraction, A is the atomic mass, ρ is the density, N_A is Avogadro's number, and $\langle \sigma v \rangle_{ij}$ is the reaction rate between species i and j .

To estimate the total contribution of a reaction to the production and destruction of a species, we calculate the average reaction flux F_{ij} over mass and time:

$$F_{ij} = \frac{1}{\delta t (m_{\text{top}} - m_{\text{bot}})} \int_{t_c}^{t_c + \delta t} \int_{m_{\text{bot}}}^{m_{\text{top}}} |f_{ij}(m, t)| dm dt$$

Using this, we can define what percentage a particular reaction contributes to the total flux for a species:

$$\langle \text{contribution} \rangle_{ij} = \frac{F_{ij}}{\sum_j F_{ij}} \quad (2)$$

calculated at $t_c = 110$ sec and $\delta t = 1$ sec. This provides quasi-equilibrium reaction fluxes at the end of the simulation.

3. RESULTS

3.1. Nucleosynthesis of the light odd-Z isotopes

The reference case is the nucleosynthesis of the light odd-Z isotopes in the O shell with the MLT-based mixing efficiency profile with an ingestion rate of $4 \times 10^{-3} M_{\odot} \text{s}^{-1}$. ^{16}O produces p , n , and α by the main O-burning reaction $^{16}\text{O} + ^{16}\text{O}$, but the ingestion of ^{12}C adds to the p , n , and α release by $^{12}\text{C} + ^{12}\text{C}$ and $^{12}\text{C} + ^{16}\text{O}$

reactions at O-burning temperatures. The sudden increase of p , n , and α increases the capture reactions (p, γ) , (n, γ) , (α, γ) , (α, p) , and (p, α) significantly which is one of the reasons why the light odd-Z elements are produced much more during the merger than the first (cf. §2.1) convective O shell.

The main reaction channels are shown in Fig. 1. Many additional reactions that are not shown as the convective-reactive nature of the O shell means different locations in the shell have varying contributions. Fig. 2 shows the isotopic mass fractions across the O shell, and as it shows the light odd-Z isotopes have a peak 1.6–1.7 M_{\odot} .

Important isotopes like ^{30}Si , $^{32,34}\text{S}$, and ^{38}Ar are created in the first convective O shell, and ^{37}Cl , ^{40}Ar , and ^{44}Ca are created in the C shell and ingested during the merger. These pathways were determined by analyzing the production of each of the species during the evolution of the C. Ritter et al. (2018b) model and the fluxes in our post-processed models. The only stable P isotope ^{31}P is produced by $^{16}\text{O}(^{16}\text{O}, p)^{31}\text{P}$. The stable Cl isotope ^{35}Cl is produced by $^{30}\text{Si}(\alpha, \gamma)^{34}\text{S}(p, \gamma)^{35}\text{Cl}$, $^{32}\text{S}(\alpha, p)^{35}\text{Cl}$, and $^{35}\text{S}(p, n)^{35}\text{Cl}$. ^{37}Cl is both ingested from the C shell and produced by $^{34}\text{S}(p, \alpha)^{37}\text{Cl}$ and $^{35}\text{Cl}(n, \gamma)^{36}\text{Cl}(n, \gamma)^{37}\text{Cl}$. The principal stable isotope of K, ^{39}K is produced by $^{38}\text{Ar}(p, \gamma)^{39}\text{K}$, the long-lived radioisotope ^{40}K is produced by $^{39}\text{K}(n, \gamma)^{40}\text{K}$, and the other stable K isotope ^{41}K is produced by $^{40}\text{K}(n, \gamma)^{41}\text{K}$ and $^{40}\text{Ar}(p, \gamma)^{41}\text{K}$. Finally, the only stable Sc isotope ^{45}Sc is produced by $^{38}\text{Ar}(\alpha, \gamma)^{42}\text{Ca}(n, \gamma)^{43}\text{Ca}(n, \gamma)^{44}\text{Ca}(p, \gamma)^{45}\text{Sc}$. However, our analysis shows that different reactions dominate the light odd-Z isotopic production depending on the mixing conditions as shown in Tables 2 and 3. Additionally, the transient before the quasi-equilibrium at the end of the simulation will have different dominant reactions, but we assume that this is not important for the final yields.

3.2. Impact of macro physics mixing on light odd-Z nucleosynthesis production

Fig. 3 shows the spread across all 24 mixing cases in overproduction in the O shell only at the end of the merger, $\text{OP} = \log_{10}(X_i/X_{i,\text{ini}})$, where X_i is the final decayed, mass-averaged mass fraction of an isotope and $X_{i,\text{ini}}$ is the initial mass fraction at the start of the merger. Over the range of mixing scenarios and entrainment rates, ^{31}P has a spread $\text{OP}_{\text{max}} - \text{OP}_{\text{min}}$ of 0.58 dex, ^{35}Cl has 1.76 dex, ^{37}Cl has 0.81 dex, ^{39}K has 2.42 dex, ^{40}K has 3.37 dex, ^{41}K has 2.31 dex, and ^{45}Sc has 1.68 dex with an average spread across all light odd-Z isotopes of 1.82 dex. The K isotopes

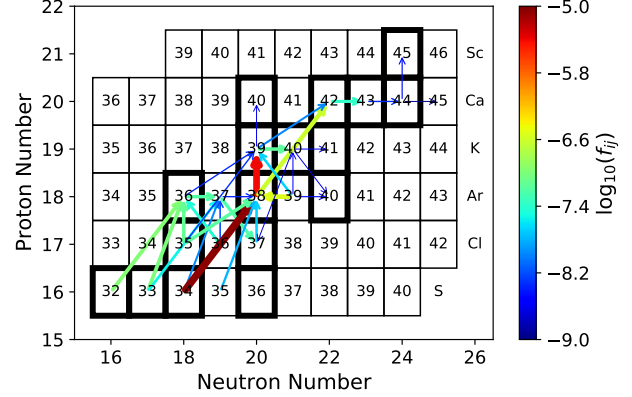


Figure 1. Chart of reactions between isotopes at $m = 1.65 M_{\odot}$ [$T = 2.231 \text{ GK}$] for the MLT mixing case with an ingestion rate of $4 \times 10^{-3} M_{\odot}\text{s}^{-1}$ at $t = 110 \text{ s}$. Both arrow colour and size indicate $\log_{10}(f_{ij})$, and arrows point in the direction of the reaction.

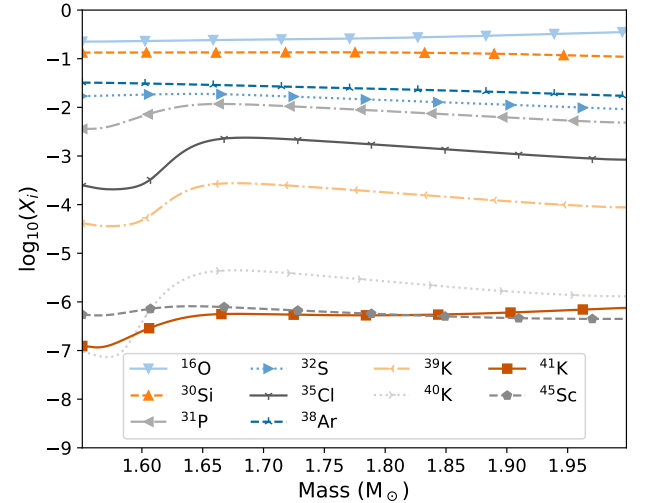


Figure 2. Isotopic mass fractions at $t = 110 \text{ s}$ without decays for the MLT mixing case with an ingestion rate of $4 \times 10^{-3} M_{\odot}\text{s}^{-1}$.

are the most affected by the mixing conditions, and ^{40}K has the largest spread of all isotopes. This underscores the importance of understanding the 3D macro physics from hydrodynamic simulations to reliably predict the final production during a merger.

Figures 4–7 show the modification to the pre-explosive yields of C. Ritter et al. (2018b) as described in §2.3. The ratios $[\text{P}/\text{Fe}]$, $[\text{Cl}/\text{Fe}]$, $[\text{K}/\text{Fe}]$, and $[\text{Sc}/\text{Fe}]$ are changed by $[-0.33, 0.23]$ dex, $[-0.84, 0.64]$ dex, $[-0.78, 1.48]$ dex, and $[-0.36, 1.29]$ dex respectively. The elemental abundances are most enhanced for the fastest ingestion rate of $4 \times 10^{-3} M_{\odot}\text{s}^{-1}$ and for the mixing cases with a downturn in the mixing efficiency. This

Isotope	$^{16}\text{O}(^{16}\text{O},p)$	(α,γ)	(α,n)	(α,p)	(p,γ)	(p,n)	(n,γ)	(γ,n)	(γ,p)	(n,p)	(n,α)	(p,α)
^{31}P	+0.97				-0.01	+0.01						
^{35}Cl		+0.01			+0.18	-0.57	+0.22		-0.01	+0.01		
^{37}Cl					+0.23	+0.07		+0.02		-0.45	+0.22	
^{39}K		+0.02			+0.04	-0.71	+0.14		-0.05	+0.01		-0.02
^{40}K				-0.09		+0.03	-0.05	+0.64	-0.09	-0.04	-0.05	
^{41}K		+0.1			-0.28	+0.24		+0.18		-0.03	-0.17	
^{45}Sc						+0.49	+0.01		-0.07	-0.42		

Table 2. Reaction fluxes contributing to the light odd-Z isotopes using Eq. (2) for the MLT mixing case with an ingestion rate of $4 \times 10^{-3} \text{ M}_\odot \text{s}^{-1}$. Contributions starting with + are productive (should be read as $i \rightarrow j$ e.g. $^{34}\text{S}(p,\gamma)^{37}\text{Cl}$ with +0.23), those starting with - are destructive (should be read as $i \leftarrow j$ e.g. $^{34}\text{S}(p,\gamma)^{35}\text{Cl}$ with -0.57), and those left blank contribute less than 1%.

Isotope	$^{16}\text{O}(^{16}\text{O},p)$	(α,γ)	(α,n)	(α,p)	(p,γ)	(p,n)	(n,γ)	(γ,n)	(γ,p)	(n,p)	(γ,α)	(n,α)	(p,α)
^{31}P	+0.91				-0.04	+0.02				-0.01			-0.01
^{35}Cl					+0.05	-0.9	+0.01			-0.03			-0.01
^{37}Cl					-0.06	+0.03				-0.52	+0.38		
^{39}K					+0.01	-0.96				-0.01			-0.01
^{40}K			-0.02	-0.03	+0.02	-0.01	+0.33	-0.02	-0.2	-0.37			
^{41}K		+0.11			-0.33	+0.2		+0.15		-0.05	-0.15	+0.01	
^{45}Sc					+0.08	+0.29		+0.01	-0.02	-0.49	+0.1		

Table 3. Reaction fluxes contributing to the light odd-Z isotopes using Eq. (2) for the $50 \times D_{3\text{D-insp.}}$ mixing case with an ingestion rate of $4 \times 10^{-3} \text{ M}_\odot \text{s}^{-1}$. Contributions starting with + are productive (should be read as $i \rightarrow j$ e.g. $^{39}\text{K}(n,\gamma)^{40}\text{K}$ with +0.33), those starting with - are destructive (should be read as $i \leftarrow j$ e.g. $^{40}\text{Ca}(n,p)^{40}\text{K}$ with -0.37), and those left blank contribute less than 1%.

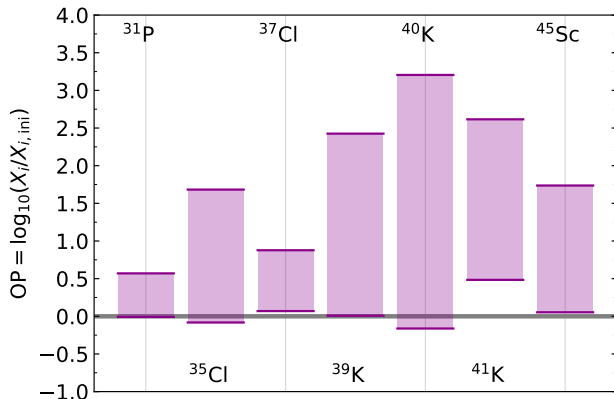


Figure 3. Overproduction of the light odd-Z isotopes for all 24 mixing cases in the O shell at 110 s. The average spread $\text{OP}_{\text{max}} - \text{OP}_{\text{min}} = 1.82$ dex, and the line at $\text{OP} = 0$ is the initial amount.

enhancement is non-monotonic with increasing convective velocities for all elements except K which is indeed most enhanced for the $50 \times D_{3\text{D-insp.}}$ mixing case.

Isotopes of the same element are not affected the same way by the mixing conditions (Fig. 3), and therefore elemental and isotopic enhancements are not necessarily

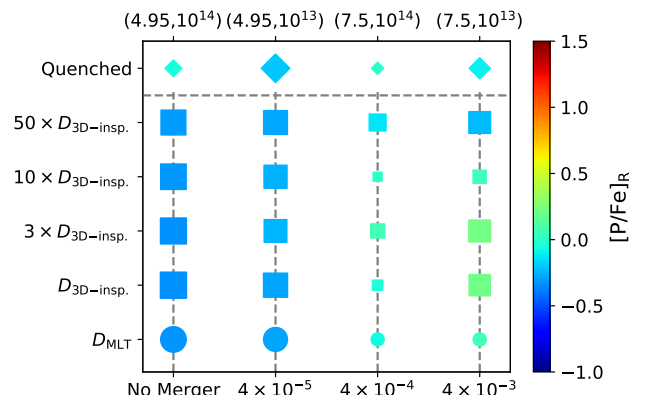


Figure 4. The change in dex for $[\text{P}/\text{Fe}]$ to the $M_{\text{ZAMS}} = 15 \text{ M}_\odot$, $Z = 0.02$ model from C. Ritter et al. (2018b) as described in §2.3. The lower x-axis is the ingestion rate in $\text{M}_\odot \text{s}^{-1}$ for the MLT (circles) and 3D-inspired mixing (squares) cases. The upper x-axis is the centre of the mixing efficiency dip in Mm and the extent of the dip in $\text{cm}^2 \text{s}^{-1}$ for the quenched (diamonds) mixing cases. Size indicates distance from $[\text{P}/\text{Fe}]_R = 0$, and colour indicates the magnitude. The C. Ritter et al. (2018b) full delayed pre-explosive yield $[\text{P}/\text{Fe}]_\odot = 2.13$ dex, and the contributions just from winds are -0.04 dex

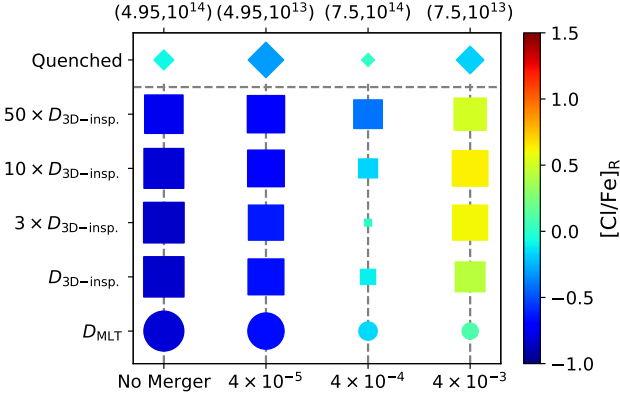


Figure 5. The same as Fig. 4 but for $[\text{Cl}/\text{Fe}]_{\text{R}}$. The C. Ritter et al. (2018b) full delayed pre-explosive yield $[\text{Cl}/\text{Fe}]_{\odot} = 2.14$ dex, and the contributions just from winds are 0.21 dex

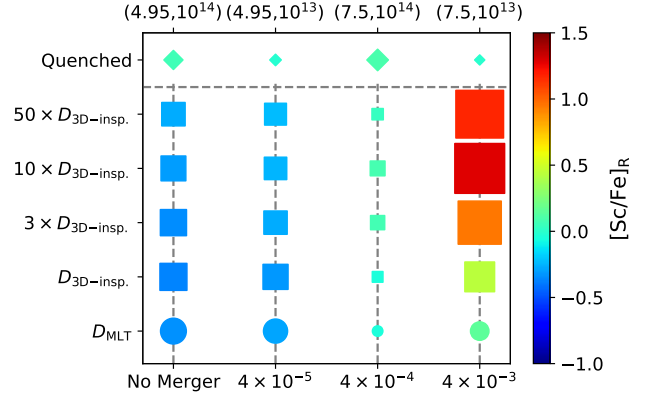


Figure 7. The same as Fig. 4 but for $[\text{Sc}/\text{Fe}]_{\text{R}}$. The C. Ritter et al. (2018b) full delayed pre-explosive yield $[\text{Sc}/\text{Fe}]_{\odot} = 1.79$ dex, and the contributions just from winds are 0.06 dex

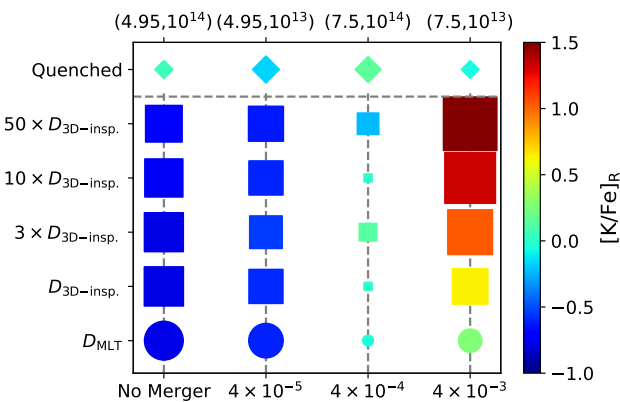


Figure 6. The same as Fig. 4 but for $[\text{K}/\text{Fe}]_{\text{R}}$. The C. Ritter et al. (2018b) full delayed pre-explosive yield $[\text{K}/\text{Fe}]_{\odot} = 1.59$ dex, and the contributions just from winds are -0.03 dex

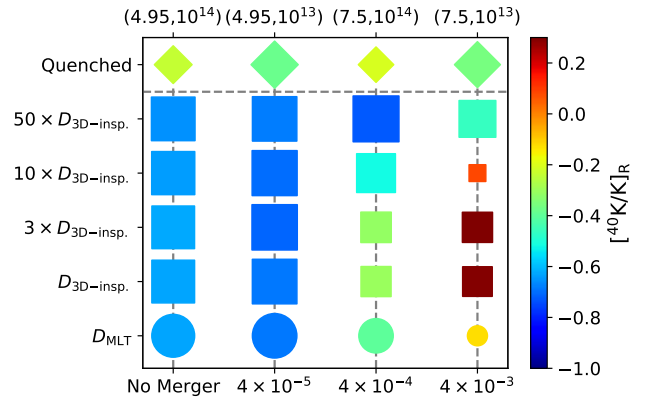


Figure 8. The same as Fig. 4 but for $[\text{K}^{40}/\text{K}]_{\text{R}}$. The C. Ritter et al. (2018b) full delayed pre-explosive yield $[\text{K}^{40}/\text{K}]_{\odot} = 1.54$ dex, and the contributions just from winds are -1.32 dex. Note that the colourbar is different from Figures 4–7.

aligned. Elemental K has the largest enhancement for the $50 \times D_{3\text{D}-\text{insp.}}$ mixing case (Fig. 6), but the isotope ^{40}K is most enhanced for the 1 and $3 \times D_{3\text{D}-\text{insp.}}$ mixing cases (Fig. 8). Elemental K is primarily ^{39}K . The enhancement of ^{40}K in the lower mixing cases implies that the mixing conditions affect how these isotopes are produced relative to each other.

Mixing conditions affect nucleosynthesis in a non-monotonic way because the O shell is a convective-reactive environment. As explored in J. Issa et al. (2025), when the mixing speeds change, so does the location of peak burning. For example, consider the reactions contributing to the ^{40}K mass fraction for the MLT

mixing case in Fig. 9 and the $50 \times D_{3\text{D}-\text{insp.}}$ mixing case in Fig. 10.

Comparing Figures 9 and 10 we see that for the faster mixing case (1) the reaction fluxes $\log_{10}(f_{ij})$ are stronger (2) the mass fractions X_i are higher and have a different shape (3) the location of the strongest reactions are deeper in the shell (4) the dominant reactions are different. In both cases, ^{40}K is both produced and destroyed by $^{39}\text{K}(n, \gamma)^{40}\text{K}$, but in the faster mixing case these reactions occur at hotter temperatures deeper in the shell and the destructive channels $^{40}\text{K}(p, n)^{40}\text{Ca}$ and $^{40}\text{K}(p, \gamma)^{41}\text{Ca}$ are much stronger. Note that ^{40}K is being net destroyed in the faster mixing case, but still has a higher mass fraction because ^{39}K is being produced even

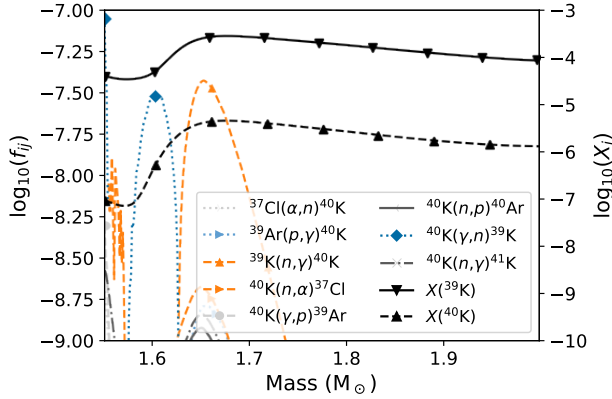


Figure 9. Reaction fluxes f_{ij} for ^{40}K and mass fractions X_i for $^{39,40}\text{K}$ for the MLT mixing case with an ingestion rate of $4 \times 10^{-3} \text{ M}_\odot \text{s}^{-1}$ at $t = 110$ s. The direction of reactions $i \rightarrow j$ are written as left to right in the legend. Note that the reaction direction notation as always left to right is different than Table 2.

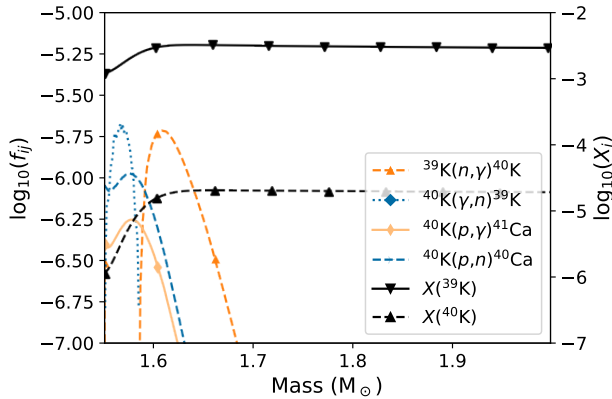


Figure 10. The same as Fig. 9 but for the $50 \times D_{3\text{D}-\text{insp.}}$ mixing case with an ingestion rate of $4 \times 10^{-3} \text{ M}_\odot \text{s}^{-1}$. Note that the reaction direction notation as always left to right is different than Table 3.

more. This is evident when comparing to Fig. 8 where the $50 \times D_{3\text{D}-\text{insp.}}$ mixing case has a lower $[^{40}\text{K}/\text{K}]$ ratio than the MLT case. Since the shell is convective-reactive, the nucleosynthesis is sensitive to the ratio of the timescales for mixing and burning which changes the location where reaction peaks occur. This behaviour is relevant for all nucleosynthesis in the O shell and is the cause of the spread in Fig. 3 and elemental abundance enhancements in Figures 4–7.

4. HETEROGENEOUS ^{40}K INTERSTELLAR MEDIUM ENRICHMENT AND IMPACT FOR ROCKY PLANET HEATING

As discussed in the previous sections, all K isotopes are efficiently produced in O-C shell mergers. It is

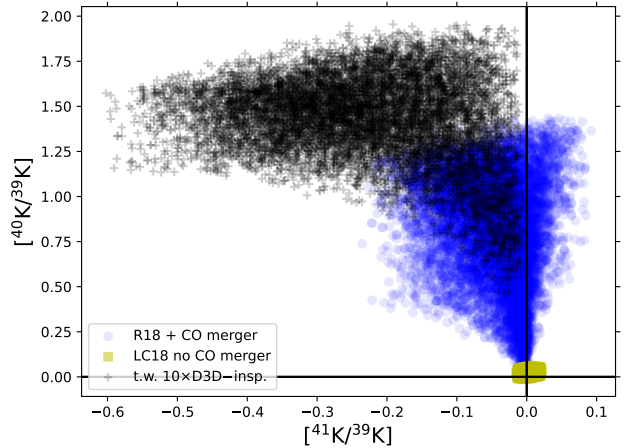


Figure 11. Predicted dispersion of K isotopic ratios in the interstellar medium (ISM) resulting from pollution by a single CCSN explosion, based on stellar yields from a 15 M_\odot star at solar metallicity with O-C shell merger (R18, C. Ritter et al. 2018a) and without (LC18 M. Limongi & A. Chieffi 2018), as well as shell-merger only predictions from this work (t.w.) for the $10 \times D_{3\text{D}-\text{insp.}}$ mixing case with an ingestion rate of $4 \times 10^{-3} \text{ M}_\odot$. Isotopic ratios are expressed in bracket notation, reported as logarithms base 10, and normalized to solar values.

known that this could reconcile the $[\text{K}/\text{Fe}]$ observations in the Milky Way disk with GCE simulations (C. Ritter et al. 2018a). ^{40}K receives the biggest boost compared to the solar scaled initial abundances. Let's consider as example the 15 M_\odot $Z = 0.02$ model by C. Ritter et al. (2018a), affected by O-C shell merger, and the analogous non-rotating model in the stellar set by M. Limongi & A. Chieffi (2018). The ^{39}K , ^{40}K and ^{41}K yields by the model with O-C shell merger are $1.959 \times 10^{-3} \text{ M}_\odot$, $1.165 \times 10^{-4} \text{ M}_\odot$ and $6.694 \times 10^{-5} \text{ M}_\odot$, respectively. The model without O-C shell merger ejects $1.061 \times 10^{-4} \text{ M}_\odot$, $6.071 \times 10^{-7} \text{ M}_\odot$ and $1.046 \times 10^{-5} \text{ M}_\odot$, respectively. While ^{39}K and ^{41}K boosts are in the order of a factor of 10 or less (C. Ritter et al. 2018a), the ^{40}K increase in our 1D model with O-C shell merger is almost 200 times larger compared to a standard CCSN production seen in the model by M. Limongi & A. Chieffi (2018). Additionally, we consider yields from our most enhanced ^{40}K production cases, the $10 \times D_{3\text{D}-\text{insp.}}$ case with an ingestion rate of $4 \times 10^{-3} \text{ M}_\odot$, which should be considered as an indicative upper limit in terms of ^{40}K yields based on the current simulations. The $10 \times D_{3\text{D}-\text{insp.}}$ case ejects $3.992 \times 10^{-2} \text{ M}_\odot$, $3.054 \times 10^{-3} \text{ M}_\odot$ and $9.857 \times 10^{-4} \text{ M}_\odot$ of ^{39}K , ^{40}K and ^{41}K , respectively.

Although this needs to be investigated further, it is likely that the occurrence of O-C shell mergers and the associated strong boost in ^{40}K takes place in a signifi-

cant fraction of but not all massive stars (C. Ritter et al. 2018a). When it happens, this is likely with variable strength. To some degree the latter is reflected by the different assumed entrainment rates. Such efficient, yet variable production can introduce a heterogeneous signature of ^{40}K in the local ISM once the CCSN explode, in addition to other K sources in GCE. In Fig. 11, we show the dispersion of K isotopic ratios in the ISM resulting from pollution by two single CCSN explosions, using the yields just provided and assuming a solar-like ISM composition. For each CCSN pollution scenario, we generated a random distribution of 10,000 points, considering a factor of 3 uncertainty in the K isotopic yields and a range of dilutions from $2 \times 10^3 \text{ M}_\odot$ (lower limit derived for a low-energy CCSN, A. P. Ji et al. 2020) to a typical value of 10^5 M_\odot of ISM material. The obtained $^{41}\text{K}/^{39}\text{K}$ dispersions are less than 10% using the model without O-C shell merger and up to about a factor of two for the model with O-C shell merger by C. Ritter et al. (2018a). Similar variations could also be expected in the solar neighborhood due to GCE effects, such as different metal enrichment histories in the disk (e.g., V. Hegedűs et al. 2025, and references therein) and stellar migration (e.g., M. Kubryk et al. 2015). If instead we consider the $10 \times D_{3\text{D}-\text{insp.}}$ mixing case presented in the previous sections, we obtain a variation up to a factor of 4 from the solar $^{41}\text{K}/^{39}\text{K}$ ratio.

On the other hand, local ISM pollution from the CCSN model by C. Ritter et al. (2018a) would generate a $^{40}\text{K}/^{39}\text{K}$ dispersion up to a factor of 20. Likewise, the $10 \times D_{3\text{D}-\text{insp.}}$ mixing case from this work would produce an even larger dispersion, up to about a factor of 100, while the model without O-C shell merger would show again an insignificant dispersion. Note, that we are showing in this way only the $10 \times D_{3\text{D}-\text{insp.}}$ mixing case, which is the one with the largest ^{40}K production but not the one with the largest $^{40}\text{K}/^{39}\text{K}$ ratio (Fig. 8). The latter is obtained for the 1 and $3 \times D_{3\text{D}-\text{insp.}}$ mixing cases.

The showcased O-C shell merger cases would introduce a strongly heterogeneous signature in the GCE K abundances of the ISM, locally decoupling the abundance of ^{40}K from the other K isotopes obtained from GCE. Consequently, the Sun cannot be used as a robust reference for the $^{40}\text{K}/\text{K}$ ratio for stars in the solar neighborhood. Instead, our work shows that solar “twins” with otherwise similar metallicity and K abundance could have significantly different initial ^{40}K abundance compared to the solar system.

The ^{40}K isotopic effect described here has important thermal histories for rocky exoplanets. Energy produced from natural radioactive decay and the leftover primor-

dial heat from planet formation powers the (internal) geodynamics of a rocky planet like Earth. Rocky planet mantle temperatures govern, for example, expressed in crustal compositions, style of (L. H. Rüpk et al. 2004) as well as tectonic regime (e.g., C. O’Neill et al. 2016; M. Brown et al. 2020)

Thermal evolution models offer a unique approach to understanding the evolution of temperatures within rocky planetary interiors (Earth, Venus, Mercury, Mars, large asteroids, icy moons, trans-neptunian objects, and ‘terrestrial-type’ exoplanets). These models are used to constrain their volcanism and surface geology. Subordinate lithophile elements such as K and Cl also help stabilize minerals that control bulk transport properties, and/or volatile transport in rocky crusts and mantles (H. Fei et al. 2017; M. Nishi et al. 2014; M. G. Pamato et al. 2015; W. Xu et al. 2008) A rocky planet’s internal heat production is a function of potential and kinetic energy released during accretion and core formation, and radioactive decay (cf. S. Labrosse & C. Jaupart 2007) thus, mantle heat production depends on planet(star) age. A planet’s ability to sustain a mantle convective regime and crustal processes changes considerably with its evolving thermal profile due to cooling over geologic timescales of billions of years (N. H. Sleep 2000). Here, we have shown that across different extrasolar systems we can expect the starting inventories of these nuclides to vary in abundance, including in their isotopes such as ^{40}K even if the elemental abundances may be similar to Solar. Despite the long-suspected (but hitherto, unconstrained) variability, the majority of exoplanet studies up to now have applied Solar values for radionuclide (U, Th, K) concentrations, often without considering the decay after planet formation (E. A. Frank et al. 2014).

As an example, we illustrate this in Fig. 12, which shows the heating rate over time for Earth. To mimic the ^{40}K variations observed in Fig. 11, we multiply and divide the current abundance of ^{40}K in Earth’s silicate mass ($3.04 \times 10^{-8} \text{ kg/kg}$, e.g. E. A. Frank et al. 2014, and references therein) by a factor of 3. Although similar terawatt (TW) values are obtained today by varying the ^{40}K abundance, the planet’s heating history would clearly be significantly different.

We will explore in detail elsewhere the implications of this for different types of rocky planets, considering more detailed pollution scenarios. Indeed, it is unclear whether the Solar System has a $^{40}\text{K}/\text{K}$ ratio consistent with GCE or if it reflects local pollution from CCSNe. Another interesting aspect, beyond the scope of this analysis, is whether we should expect local variations in the other radioactive sources, U and Th. The current GCE of Th in the Milky Way disk is under de-

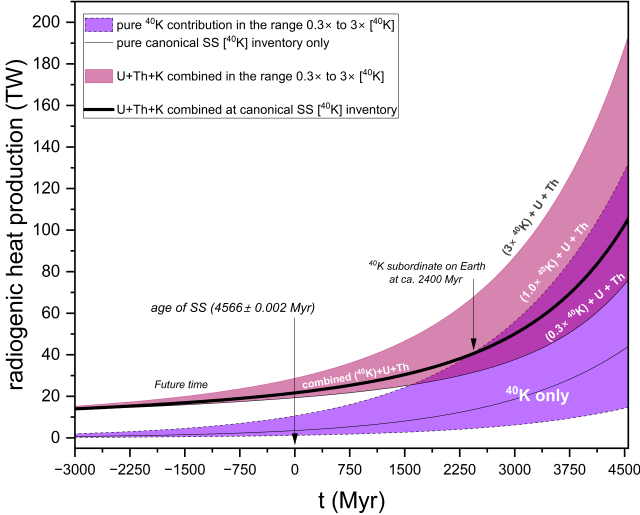


Figure 12. The evolution over time of the radioactive heat production is shown for an Earth-like planet, where ^{40}K abundances are increased and decreased by a factor of 3 compared to the typical Earth values. The combined total heat productions by ^{40}K , ^{232}Th , ^{235}U , and ^{238}U are also shown. Time on the x-axis is in Myr before present and so moves from right to left. Negative values on the x-axis refer to future time.

bate (e.g., R. B. Botelho et al. 2019; T. Mishenina et al. 2022), while measuring U in stellar spectra is even more challenging. Since *r*-process sources are expected to be much rarer than CCSNe (e.g., C. Sneden et al. 2008; J. J. Cowan et al. 2021), heterogeneous signatures from local $^{235,238}\text{U}$ and ^{232}Th pollution are likely to be extremely rare and possibly directly associated with the stellar Th abundance. However, the relevance of such heterogeneity affecting also the *r*-process actinide abundances cannot be ruled out. It is worth noting that a significant ^{244}Pu abundance enhancement, where ^{244}Pu is a short-lived radioactive isotope also made by the *r* process, can be inferred for the Early Solar System compared to measurements representative of the present ISM, derived from deep-sea crust and other planetary materials (e.g., K. Hotokezaka et al. 2015; A. Wallner et al. 2021; B. Wehmeyer et al. 2023; X. Wang et al. 2023; S. Bishop et al. 2025).

5. DISCUSSIONS AND CONCLUSIONS

As shown in this analysis, O-C shell mergers significantly modify the pre-explosive yields of the light odd-Z elements, particularly elemental K which can be enhanced by up to $38\times$ compared to C. Ritter et al. (2018b). These results reflect the systematic uncertainty in 1D stellar models due to the treatment of mixing, and highlight the potential intrinsic variability in massive stars. This indicates the importance for 3D hydrody-

namic simulations to constrain the mixing conditions during these events to improve predictions. We have previously shown that mixing scenario changes which reaction rates are correlated with isotopic production (J. Issa et al. 2025), so with realistic 3D mixing conditions the next critical step is to explore the uncertainties in these rates. Observations can provide constraints, such as those that report a low dispersion in [K/Fe] for metal-poor stars (e.g., S. M. Andrievsky et al. 2010; J. G. Cohen et al. 2013; I. U. Roederer et al. 2014; M. N. Ishigaki et al. 2025). This could indicate that mixing conditions are more uniform in real stars than the range explored here, however GCE calculations that include a realistic range of shell merger conditions are needed to confirm this. C. Ritter et al. (2018a) show that O-C shell mergers are necessary to explain the light odd-Z elements in GCE, but L. Roberti et al. (2025) show that this could also lead to models producing more than observations. Future 3D modelling will be needed to define the correct mixing conditions, possibly yielding K abundances compatible with both stellar archaeology and GCE. Finally, because the O shell is convective-reactive, the variations in yields due to mixing may not be the same for models with different temperature profiles or shell sizes. Therefore, the results presented here cannot be extrapolated to other stellar models without further study.

Mixing conditions are set by the 3D macro physics of convection of the O-C shell merger and strongly affects the production of ^{40}K , which is a long-lived radionuclide with a half-life of $t_{1/2} = 1.248$ Gyr that contributes to radiogenic heating in planets (E. A. Frank et al. 2014; C. O'Neill et al. 2020). Not only is the elemental K enhanced, but so is $[^{40}\text{K}/\text{Fe}]$ up to $26\times$ compared to C. Ritter et al. (2018b) result for the $10 \times D_{3\text{D}-\text{insp.}}$ mixing case with an ingestion rate of $4 \times 10^{-3} \text{ M}_\odot \text{s}^{-1}$ (using square bracket notation adding the results of Fig. 6 and Fig. 8). This would mean that the ^{40}K contributed to GCE is significantly enhanced. As we showed in Fig. 11, there is a large variation in the $^{40}\text{K}/^{39}\text{K}$ ratio which tracks the $^{40}\text{K}/\text{K}$ ratio as ^{39}K is the dominant isotope of K. This combined with the fact that the mixing conditions do not non-monotonically affect the production of ^{39}K and ^{40}K means that the $^{40}\text{K}/^{39}\text{K}$ ratio can vary significantly between stars with otherwise similar metallicity and elemental K observations, which brings into question the validity of deriving ^{40}K from an elemental abundance measurement of the host star. Furthermore, we have shown that the production of ^{40}K in O-C shell mergers is so high that it could potentially introduce heterogeneous signatures in the local ISM. With the reference CCSN model considered in this work, we find that ^{40}K could be enhanced by up to a factor of 20 com-

pared to its background GCE abundance, decoupling the ^{40}K abundance from the observable K abundances resulting from GCE. With the most ^{40}K -rich mixing model discussed in this work, we find possible heterogeneous signatures affecting all K isotopes, with a ^{40}K -enhancement up to a factor of a hundred.

An enhanced ^{40}K would have a significant effect on the history of radiogenic heat production in the mantle of an Earth-like planet. A higher initial inventory of ^{40}K raises the radiogenic heat budget and sustains vigorous mantle convection and melt production for longer, which in turn prolongs outgassing and delays tectonic/volcanic shutdown. Thermal-chemical evolution models show that increased internal heating can keep silicate planets volcanically and climatically active for Gyr timescales beyond nominal cases by maintaining continuous outgassed supply to the atmosphere and postponing secular cooling (E. A. Frank et al. 2014). In our context, a $\sim 3\times$ enhancement in ^{40}K plausibly extends the duration of high outgassing and temperate surface conditions into later epochs relative to an Earth twin, while a $\sim 10\times$ case would push the system toward a long-lived super-volcanic regime (still buffered by the carbon-silicate feedback), thereby broadening the temporal window for habitability via sustained greenhouse forcing and volatile cycling (B. J. Foley & A. J. Smye 2018).

An elevated ^{40}K budget implies persistently high volcanic fluxes and a greater frequency of large eruptions. Time-variable outgassing (e.g., SO_2 pulses that rapidly convert to sulfate aerosols) imprints may be detectable, *time-dependent* changes in atmospheric composition—most notably in O_3 and H_2O bands—on Earth-like exoplanets (C. M. Ostberg et al. 2023). Multi-epoch direct imaging/spectroscopy with future facilities such as the Habitable Worlds Observatory may therefore have the potential to discriminate a super-volcanic, high- ^{40}K Earth-analog from a more quiescent twin (P. Liggins et al. 2022b; C. M. Ostberg et al. 2023).

Although our results demonstrate that mixing conditions strongly influence the production of the light odd-Z elements, they do not yet provide a complete picture. Our analysis examines a single stellar model at $Z = 0.02$. The $^{39-41}\text{K}$ mass fractions can vary by factors of 3, 16, and 38 respectively in the merged O-C shells listed in Table 1. Model differences are not as impactful as mixing conditions, however, as §3.2 shows that final production of ^{39}K , ^{40}K , and ^{41}K in the O shell can vary by factors of 263, 2340, and 204 respectively across all mixing cases.

Our results in Figures 4–8 omit the subsequent core-collapse supernova and any explosive nucleosynthesis

that may occur, and uses a first-order approximation to estimate the final yields. The post-processing approach does not properly account for the evolution of the merger in the 1D model, as temperature and density evolve and we do not simulate the mixing of material in the O shell up into the merged C shell. Further, it is not clear what the length of the merger would be in 3D nor its behaviour for energy feedback in response to the burning of ingested fuel, such as the recently identified SPA process (L. Roberti & M. Pignatari 2025). While these approximations limit presently the accuracy of specific quantitative predictions, the result presented here, that 3D macro physics mixing conditions strongly affect the nucleosynthesis, is robust. We also demonstrated that the 1D mixing prescriptions used here do not capture the full range of possible mixing behaviours that may occur in 3D.

Additionally, one would expect the MLT $4 \times 10^{-3} \text{ M}_\odot \text{s}^{-1}$ mixing case to match the C. Ritter et al. (2018b) model most closely in Figures 4–8. The difference results from a combination of the above factors and possibly also that in our targeted, zoom-in post-processing we took great care that temporal and spatial resolution is sufficient to resolve the convective-reactive nucleosynthesis, which cannot be expected from survey stellar evolution models as those by C. Ritter et al. (2018b). This highlights the difficulty of capturing convective-reactive events in 1D stellar evolution models and the need for 3D hydrodynamic simulations to inform 1D models.

The highest priority, therefore, is to investigate the macro physics of O-C shell mergers with fully 3D hydrodynamic simulations. Such simulations must quantify the mixing, identify feedback mechanisms, and establish when and how often mergers occur. Ultimately, full stellar-evolution calculations with mixing prescriptions calibrated to these 3D simulations are needed to assess the impact of mixing conditions on pre-supernova and ejecta yields, and inform planetary science studies of the impact of ^{40}K on planetary thermal histories.

ACKNOWLEDGMENTS

FH is supported by a Natural Sciences and Engineering Research Council of Canada (NSERC) Discovery Grant and acknowledges support from the NSERC award SAPPJ-797 2021-00032 *Nuclear physics of the dynamic origin of the elements*. We acknowledge support from the ChETEC-INFRA project funded by the European Union’s Horizon 2020 Research and Innovation programme (Grant Agreement No 101008324). This research has used

the Astrohub online virtual research environment (<https://astrohub.uvic.ca>), developed and operated by the Computational Stellar Astrophysics group at the University of Victoria and hosted on the Digital Research Alliance of Canada Arbutus Cloud at the University of Victoria. This work benefited from interactions and workshops co-organized by The Center for Nuclear astrophysics Across Messengers (CeNAM) which is supported by the U.S. Department of Energy, Office of Science, Office of Nuclear Physics, under Award Number DE-SC0023128. MP acknowledges the support to NuGrid from the “Lendület-2023” Program of the Hungarian Academy of Sciences (LP2023-10, Hungary), the ERC Consolidator Grant funding scheme (Project RADIOSTAR, G.A. n. 724560, Hungary), the ChETEC COST Action (CA16117), supported by the European Cooperation in Science and Technology, and the IReNA network supported by NSF AccelNet (Grant No. OISE-1927130). MP also thanks the support from NKFI via K-project 138031 (Hungary). SJM and MP acknowledge funding from the ERC Horizon Europe funding

programme in support of the Synergy Grant - Geoastronomy, grant agreement number 101166936. SJM also thanks the BGI/University of Bayreuth in Germany for hosting the Geoastronomy Research Group.

AUTHOR CONTRIBUTIONS

JI performed the simulations, analyzed the results, and wrote the manuscript. FH provided guidance and support for the project and edited the manuscript. MP calculated the impact of heterogeneous mixing in the ISM of K isotopes, participating in data analysis and in writing the manuscript. SM computed the differential heat production of variable starting ^{40}K abundances, participating in data analysis, and in writing the manuscript.

Software: The data and analysis tools are available on Zenodo under an open-source Creative Commons Attribution license: [doi:10.5281/zenodo.1757602](https://doi.org/10.5281/zenodo.1757602). They are also available for download from the NuGrid collaboration website: download.nugridstars.org.

REFERENCES

Andrassy, R., Herwig, F., Woodward, P., & Ritter, C. 2020, Monthly Notices of the Royal Astronomical Society, 491, 972, doi: [10.1093/mnras/stz2952](https://doi.org/10.1093/mnras/stz2952)

Andrievsky, S. M., Spite, M., Korotin, S. A., et al. 2010, Astronomy and Astrophysics, 509, A88, doi: [10.1051/0004-6361/200913223](https://doi.org/10.1051/0004-6361/200913223)

Asplund, M., Grevesse, N., Sauval, A. J., & Scott, P. 2009, Annual Review of Astronomy and Astrophysics, 47, 481, doi: [10.1146/annurev.astro.46.060407.145222](https://doi.org/10.1146/annurev.astro.46.060407.145222)

Bishop, S., Stanciu, I., Cabré, A., et al. 2025, PSJ, 6, 75, doi: [10.3847/PSJ/adbbd6](https://doi.org/10.3847/PSJ/adbbd6)

Botelho, R. B., Milone, A. d. C., Meléndez, J., et al. 2019, MNRAS, 482, 1690, doi: [10.1093/mnras/sty2791](https://doi.org/10.1093/mnras/sty2791)

Brown, M., Johnson, T., & Gardiner, N. J. 2020, Annual Review of Earth and Planetary Sciences, 48, 291, doi: [10.1146/annurev-earth-081619-052705](https://doi.org/10.1146/annurev-earth-081619-052705)

Cohen, J. G., Christlieb, N., Thompson, I., et al. 2013, The Astrophysical Journal, 778, 56, doi: [10.1088/0004-637X/778/1/56](https://doi.org/10.1088/0004-637X/778/1/56)

Cowan, J. J., Sneden, C., Lawler, J. E., et al. 2021, Reviews of Modern Physics, 93, 015002, doi: [10.1103/RevModPhys.93.015002](https://doi.org/10.1103/RevModPhys.93.015002)

Davis, A., Jones, S., & Herwig, F. 2018, Monthly Notices of the Royal Astronomical Society, 484, 3921, doi: [10.1093/mnras/sty3415](https://doi.org/10.1093/mnras/sty3415)

Fei, H., Huang, R., & Yang, X. 2017, Geophysical Research Letters, 44, 10226, doi: [10.1002/2017GL075070](https://doi.org/10.1002/2017GL075070)

Fields, C. E., & Couch, S. M. 2021, The Astrophysical Journal, 921, 28, doi: [10.3847/1538-4357/ac24fb](https://doi.org/10.3847/1538-4357/ac24fb)

Fischer, T. P., & Aiuppa, A. 2020, Annual Review of Earth and Planetary Sciences, 48, 529, doi: [10.1146/annurev-earth-053018-060321](https://doi.org/10.1146/annurev-earth-053018-060321)

Foley, B. J., & Smye, A. J. 2018, Astrobiology, 18, 873, doi: [10.1089/ast.2017.1695](https://doi.org/10.1089/ast.2017.1695)

Frank, E. A., Meyer, B. S., & Mojzsis, S. J. 2014, Icarus, 243, 274, doi: [10.1016/j.icarus.2014.08.031](https://doi.org/10.1016/j.icarus.2014.08.031)

Frank, E. A., Meyer, B. S., & Mojzsis, S. J. 2014, Icarus, 243, 274, doi: [10.1016/j.icarus.2014.08.031](https://doi.org/10.1016/j.icarus.2014.08.031)

Frank, E. A., Meyer, B. S., & Mojzsis, S. J. 2014, Icarus, 243, 274, doi: [10.1016/j.icarus.2014.08.031](https://doi.org/10.1016/j.icarus.2014.08.031)

Freytag, B., Ludwig, H. G., & Steffen, M. 1996, Astronomy and Astrophysics, 313, 497

Fryer, C. L., Belczynski, K., Wiktorowicz, G., et al. 2012, The Astrophysical Journal, 749, 91, doi: [10.1088/0004-637X/749/1/91](https://doi.org/10.1088/0004-637X/749/1/91)

Hegedűs, V., Mészáros, S., Világos, B., et al. 2025, A&A, 699, A293, doi: [10.1051/0004-6361/202553951](https://doi.org/10.1051/0004-6361/202553951)

Herwig, F. 2000, The Evolution of AGB Stars with Convective Overshoot, arXiv, doi: [10.48550/arXiv.astro-ph/0007139](https://doi.org/10.48550/arXiv.astro-ph/0007139)

Herwig, F., Woodward, P. R., Lin, P.-H., Knox, M., & Fryer, C. 2014, The Astrophysical Journal Letters, 792, L3, doi: [10.1088/2041-8205/792/1/L3](https://doi.org/10.1088/2041-8205/792/1/L3)

Hotokezaka, K., Piran, T., & Paul, M. 2015, *Nature Physics*, 11, 1042, doi: [10.1038/nphys3574](https://doi.org/10.1038/nphys3574)

Ishigaki, M. N., Tominaga, N., Aoki, W., et al. 2025, Potassium Abundances in Extremely Metal Poor Stars: Implications for Nucleosynthesis in the Final Stages of Massive Star Evolution, arXiv, doi: [10.48550/arXiv.2508.20484](https://doi.org/10.48550/arXiv.2508.20484)

Issa, J., Herwig, F., Denissenkov, P., & Pignatari, M. 2025, Impact of 3D Macro Physics and Nuclear Physics on the p Nuclei in O-C Shell Mergers, arXiv, doi: [10.48550/arXiv.2507.16965](https://doi.org/10.48550/arXiv.2507.16965)

Ji, A. P., Li, T. S., Simon, J. D., et al. 2020, *ApJ*, 889, 27, doi: [10.3847/1538-4357/ab6213](https://doi.org/10.3847/1538-4357/ab6213)

Jones, S., Andrassy, R., Sandalski, S., et al. 2017, *Monthly Notices of the Royal Astronomical Society*, 465, 2991, doi: [10.1093/mnras/stw2783](https://doi.org/10.1093/mnras/stw2783)

Kobayashi, C., Karakas, A. I., & Lugaro, M. 2020, *The Astrophysical Journal*, 900, 179, doi: [10.3847/1538-4357/abae65](https://doi.org/10.3847/1538-4357/abae65)

Korenaga, J. 2008, *Terra Nova*, 20, 419, doi: [10.1111/j.1365-3121.2008.00843.x](https://doi.org/10.1111/j.1365-3121.2008.00843.x)

Kubryk, M., Prantzos, N., & Athanassoula, E. 2015, *A&A*, 580, A126, doi: [10.1051/0004-6361/201424171](https://doi.org/10.1051/0004-6361/201424171)

Labrosse, S., & Jaupart, C. 2007, *Earth and Planetary Science Letters*, 260, 465, doi: [10.1016/j.epsl.2007.05.046](https://doi.org/10.1016/j.epsl.2007.05.046)

Liggins, P., Jordan, S., Rimmer, P. B., & Shorttle, O. 2022a, *Journal of Geophysical Research: Planets*, 127, e2021JE007123, doi: [10.1029/2021JE007123](https://doi.org/10.1029/2021JE007123)

Liggins, P., Jordan, S., Rimmer, P. B., & Shorttle, O. 2022b, *Journal of Geophysical Research: Planets*, 127, e2021JE007123, doi: [10.1029/2021JE007123](https://doi.org/10.1029/2021JE007123)

Limongi, M., & Chieffi, A. 2018, *ApJS*, 237, 13, doi: [10.3847/1538-4365/aacb24](https://doi.org/10.3847/1538-4365/aacb24)

Meakin, C. A., & Arnett, D. 2006, *The Astrophysical Journal*, 637, L53, doi: [10.1086/500544](https://doi.org/10.1086/500544)

Meakin, C. A., & Arnett, D. 2007, *The Astrophysical Journal*, 667, 448, doi: [10.1086/520318](https://doi.org/10.1086/520318)

Mishenina, T., Pignatari, M., Gorbaneva, T., et al. 2022, *MNRAS*, 516, 3786, doi: [10.1093/mnras/stac2361](https://doi.org/10.1093/mnras/stac2361)

Mishenina, T., Pignatari, M., Côté, B., et al. 2017, *MNRAS*, 469, 4378, doi: [10.1093/mnras/stx1145](https://doi.org/10.1093/mnras/stx1145)

Nishi, M., Irifune, T., Tsuchiya, J., et al. 2014, *Nature Geoscience*, 7, 224, doi: [10.1038/NGEO2074](https://doi.org/10.1038/NGEO2074)

Noack, L., & Breuer, D. 2014, *Planetary and Space Science*, 98, 41, doi: [10.1016/j.pss.2013.06.020](https://doi.org/10.1016/j.pss.2013.06.020)

O'Neill, C., Lenardic, A., Weller, M., et al. 2016, *Physics of the Earth and Planetary Interiors*, 255, 80, doi: [10.1016/j.pepi.2016.04.002](https://doi.org/10.1016/j.pepi.2016.04.002)

O'Neill, C., Lowman, J., & Wasiliev, J. 2020, *Icarus*, 352, 114025, doi: [10.1016/j.icarus.2020.114025](https://doi.org/10.1016/j.icarus.2020.114025)

Ortenzi, G., Noack, L., Sohl, F., et al. 2020, *Scientific Reports*, 10, 10907, doi: [10.1038/s41598-020-67751-7](https://doi.org/10.1038/s41598-020-67751-7)

Ostberg, C. M., Guzewich, S. D., Kane, S. R., et al. 2023, *AJ*, 166, 199, doi: [10.3847/1538-3881/acfe12](https://doi.org/10.3847/1538-3881/acfe12)

Pamato, M. G., Myhill, R., Ballaran, T. B., et al. 2015, *Nature Geoscience*, 8, 75, doi: [10.1038/NGEO2306](https://doi.org/10.1038/NGEO2306)

Paxton, B., Bildsten, L., Dotter, A., et al. 2010, *The Astrophysical Journal Supplement Series*, 192, 3, doi: [10.1088/0067-0049/192/1/3](https://doi.org/10.1088/0067-0049/192/1/3)

Pignatari, M., Herwig, F., Hirschi, R., et al. 2016, *The Astrophysical Journal Supplement Series*, 225, 24, doi: [10.3847/0067-0049/225/2/24](https://doi.org/10.3847/0067-0049/225/2/24)

Prantzos, N., Abia, C., Limongi, M., Chieffi, A., & Cristallo, S. 2018, *MNRAS*, 476, 3432, doi: [10.1093/mnras/sty316](https://doi.org/10.1093/mnras/sty316)

Rauscher, T., Heger, A., Hoffman, R. D., & Woosley, S. E. 2002, *The Astrophysical Journal*, 576, 323, doi: [10.1086/341728](https://doi.org/10.1086/341728)

Ritter, C., Andrassy, R., Côté, B., et al. 2018a, *Monthly Notices of the Royal Astronomical Society*, 474, L1, doi: [10.1093/mnras/slx126](https://doi.org/10.1093/mnras/slx126)

Ritter, C., Herwig, F., Jones, S., et al. 2018b, *Monthly Notices of the Royal Astronomical Society*, 480, 538, doi: [10.1093/mnras/sty1729](https://doi.org/10.1093/mnras/sty1729)

Rizzuti, F., Hirschi, R., Varma, V., et al. 2024, *Monthly Notices of the Royal Astronomical Society*, 533, 687, doi: [10.1093/mnras/stae1778](https://doi.org/10.1093/mnras/stae1778)

Roberti, L., & Pignatari, M. 2025, The SPAr Process: Proton Captures Powering Carbon-Oxygen Shell Mergers in Massive Stars, doi: [10.48550/arXiv.2509.13749](https://doi.org/10.48550/arXiv.2509.13749)

Roberti, L., Pignatari, M., Brinkman, H. E., et al. 2025, The Occurrence and Impact of Carbon-Oxygen Shell Mergers in Massive Stars, arXiv

Roederer, I. U., Preston, G. W., Thompson, I. B., et al. 2014, *The Astronomical Journal*, 147, 136, doi: [10.1088/0004-6256/147/6/136](https://doi.org/10.1088/0004-6256/147/6/136)

Rüpke, L. H., Morgan, J. P., Hört, M., & Connolly, J. A. D. 2004, 223, 17, doi: [10.1016/j.epsl.2004.04.018](https://doi.org/10.1016/j.epsl.2004.04.018)

Sleep, N. H. 2000, *Journal of Geophysical Research: Planets*, 105, 17563, doi: [10.1029/2000JE001240](https://doi.org/10.1029/2000JE001240)

Sneden, C., Cowan, J. J., & Gallino, R. 2008, *ARA&A*, 46, 241, doi: [10.1146/annurev.astro.46.060407.145207](https://doi.org/10.1146/annurev.astro.46.060407.145207)

Spaargaren, R. J., Wang, H. S., Mojzsis, S. J., Ballmer, M. D., & Tackley, P. J. 2023, *The Astrophysical Journal*, 948, 53, doi: [10.3847/1538-4357/acac7d](https://doi.org/10.3847/1538-4357/acac7d)

Wallner, A., Froehlich, M. B., Hotchkis, M. A. C., et al. 2021, *Science*, 372, 742, doi: [10.1126/science.aax3972](https://doi.org/10.1126/science.aax3972)

Wang, X., Clark, A. M., Ellis, J., et al. 2023, *ApJ*, 948, 113, doi: [10.3847/1538-4357/acbeaa](https://doi.org/10.3847/1538-4357/acbeaa)

Wehmeyer, B., López, A. Y., Côté, B., et al. 2023, ApJ, 944, 121, doi: [10.3847/1538-4357/acafec](https://doi.org/10.3847/1538-4357/acafec)

Xu, W., Lithgow-Bertelloni, C., Stixrude, L., & Ritsema, J. 2008, Earth and Planetary Science Letters, 275, 70, doi: [10.1016/j.epsl.2008.08.012](https://doi.org/10.1016/j.epsl.2008.08.012)

Yadav, N., Müller, B., Janka, H. T., Melson, T., & Heger, A. 2020, The Astrophysical Journal, 890, 94, doi: [10.3847/1538-4357/ab66bb](https://doi.org/10.3847/1538-4357/ab66bb)

Yoshida, T., Takiwaki, T., Aguilera-Dena, D. R., et al. 2021, Monthly Notices of the Royal Astronomical Society, 506, L20, doi: [10.1093/mnrasl/slab067](https://doi.org/10.1093/mnrasl/slab067)

Yoshida, T., Takiwaki, T., Kotake, K., et al. 2019, The Astrophysical Journal, 881, 16, doi: [10.3847/1538-4357/ab2b9d](https://doi.org/10.3847/1538-4357/ab2b9d)